

# We are IntechOpen, the world's leading publisher of Open Access books Built by scientists, for scientists

6,900

Open access books available

186,000

International authors and editors

200M

Downloads

Our authors are among the

154

Countries delivered to

TOP 1%

most cited scientists

12.2%

Contributors from top 500 universities



WEB OF SCIENCE™

Selection of our books indexed in the Book Citation Index  
in Web of Science™ Core Collection (BKCI)

Interested in publishing with us?  
Contact [book.department@intechopen.com](mailto:book.department@intechopen.com)

Numbers displayed above are based on latest data collected.  
For more information visit [www.intechopen.com](http://www.intechopen.com)



# Compliant Tactile Sensors for High-Aspect-Ratio Form Metrology

Erwin Peiner

*Technische Universität Carolo-Wilhelmina zu Braunschweig  
Germany*

## 1. Introduction

Robust manufacturing of micro parts at high throughput needs tailored concepts and methods to assure unchanging work piece quality. An actual challenge is the dimensional metrology with meso-to-microscopic high-aspect ratio features of micro-system components, e.g. micro gears for watches and micro motors, ferrules of optical fibers, hollow microneedles for painless drug delivery into living cells, planar reflective lenses for X-ray optics, densely packed arrays of square channels in lobster-eye optics and through silicon vias (TSV) for vertical electrical interconnects of 3D integrated micro systems and circuits (Baron et al., 2008; Engelke et al., 2007; Hon et al., 2005; Li et al., 2007; Meyer et al., 2008; Muralikrishnan et al., 2005; Simon et al., 2008; Vora et al., 2008; Weckenmann et al., 2006). Form and roughness of deep and narrow micro holes play an important role for the function of nozzles designed for liquid injection. The inlet roundness of the hole, e. g., mainly determines whether flow is detached from the wall resulting in a constricted liquid jet or the fluid is atomized into small droplets. Detached flow can be observed with hydroentangling nozzles of 80 to 150  $\mu\text{m}$  in diameter and 1 mm in depth (Anantharamaiah et al., 2007) while in the case of fuel injection nozzles atomization of the fluid occurs. The form of the spray holes was found to be crucial for optimal fuel injection, i.e. for combustion at low consumption and exhaust gas emission (Jung et al., 2008). Diameter, surface roughness, and inlet chamfer radius have a direct influence on fuel spray atomization, air entrainment and fuel-air mixing. Improved fuel economy, better soot oxidation and reduced NO<sub>x</sub> emission are benefits observed at optimized hole machining conditions. Furthermore, fuel penetration and spray angle were found to depend on the conicity of the hole which is attributed to the fuel atomization near the hole exit (Bae et al. 2002).

While several techniques exist for micro deep hole machining at high throughput, e. g., micro drilling, electro-discharge machining (EDM), laser beam machining (LBM) and deep reactive ion etching (DRIE) (Diver et al., 2004; Hon et al., 2005; Jung et al., 2007; Krüger et al., 2007; Li et al., 2007; Seo et al., 2008), access to the inside surface of deep and narrow micro holes for metrology is very limited. In Fig. 1 the schematic and scanning electron microscopy (SEM) photographs of the seat of a VCO (valve covered orifice) of direct injection (DI) Diesel engine nozzle is shown comprising six spray holes which are 1.1-mm-deep and have a diameter of 165  $\mu\text{m}$ . In the right part of this figure a close-up of one hole by SEM as well as by digital microscopy are shown which display the nozzle surface around

Source: Sensors, Focus on Tactile, Force and Stress Sensors, Book edited by: Jose Gerardo Rocha and Senentxu Lanceros-Mendez, ISBN 978-953-7619-31-2, pp. 444, December 2008, I-Tech, Vienna, Austria

the outlet edge of the hole but give only a vague impression of form and roughness of the near-edge inner surface. Form measurement of the inside surface profile or topography requires either sectioning of the nozzle along its axis or impressing the hole with a polymer, which is destructive and/or time-consuming (Anantharamaiah et al., 2007; Baron et al., 2008; Cusanelli et al., 2007; Diver et al., 2004; Hon et al., 2005; Jung et al., 2007; Jung et al., 2008; Krüger et al., 2007). Novel metrological tools are required for fast and non-destructive form and roughness measurements of spray holes, which enable an in-process control of the hole machining parameters under the constraints of batch fabrication at high throughput. Measurement resolution and uncertainty in the nanometer range are needed over a millimeter length scale within a laterally constricted volume of hundred microns in diameter showing that form measurement inside spray holes is a typical example for micro/nano metrology.

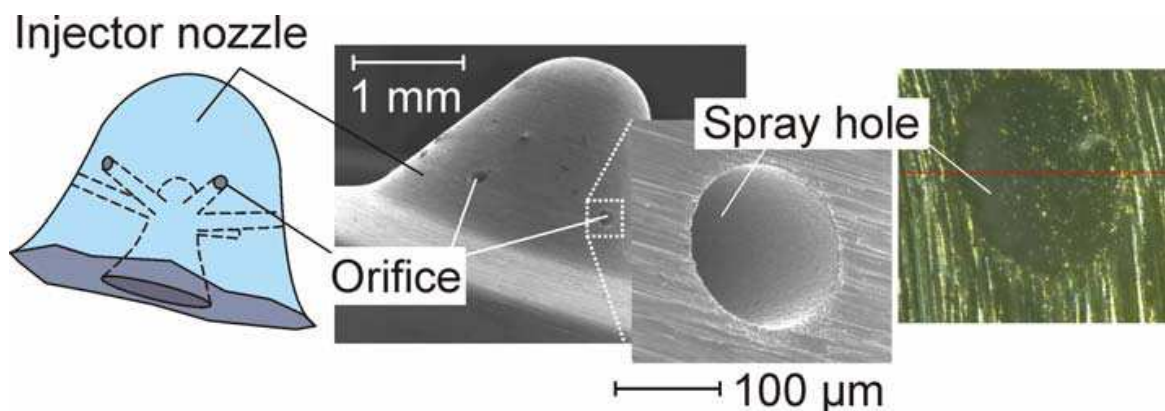


Fig. 1. Schematic (left) and scanning electron microscopy (SEM) photograph (middle) of the round end of a VCO DI Diesel nozzle. In the right part the SEM photograph and a digital optical microphotograph of one spray hole are shown at higher magnifications.

In recent years coordinate measuring machines (CMM) have been constructed for direct metrological characterization of high aspect-ratio microstructures (Bos et al., 2004; Bos et al., 2007; Küng et al., 2007; Peggs et al., 1999; Seitz, 2005; Tibrewala et al., 2008). For narrow holes actively sensing probing elements were developed which were scaled down to diameters of 120 - 300  $\mu\text{m}$ . A schematic of such a type of 3D micro probe is displayed in Fig. 2a. The membrane supporting the shank comprises the stress sensing elements which indicate the position of the probing sphere. Further reduction of the probe diameter is only feasible with simultaneous reduction of the shaft length, i. e. to avoid bending of the probing shaft, its length-to-diameter ratio is limited.

Alternative concepts of tactile micro probe sensors have been proposed and tested based on a compliant instead of a stiff shaft (Table 1). Passive-sensing fiber-optic and vibrating carbon probes comprising either a small glass sphere (Fig. 2b, Cusanelli et al., 2007; Kao & Shih, 2007; Rauh, 2005; UMAP, 2008) or a "virtual tip" (Fig. 2c, Bauza et al., 2005; Woody & Bauza, 2007) as the probing element offer very low probing forces around 1  $\mu\text{N}$  and less. However, the specified uncertainty is rather limited, only for the virtual-tip probe a repeatability of  $\sim 10$  nm is reported (Woody & Bauza, 2007). A severe disadvantage is the probing speed of few tens of pts/s or few tens of  $\mu\text{m/s}$  which is too slow for high-throughput form and roughness measurements (Cusanelli et al., 2007). Furthermore, the diameter of the probing sphere, which is 74  $\mu\text{m}$  in the case of the glass fiber probe (Kao & Shih, 2007), is yet a limitation for the accessible hole diameter.

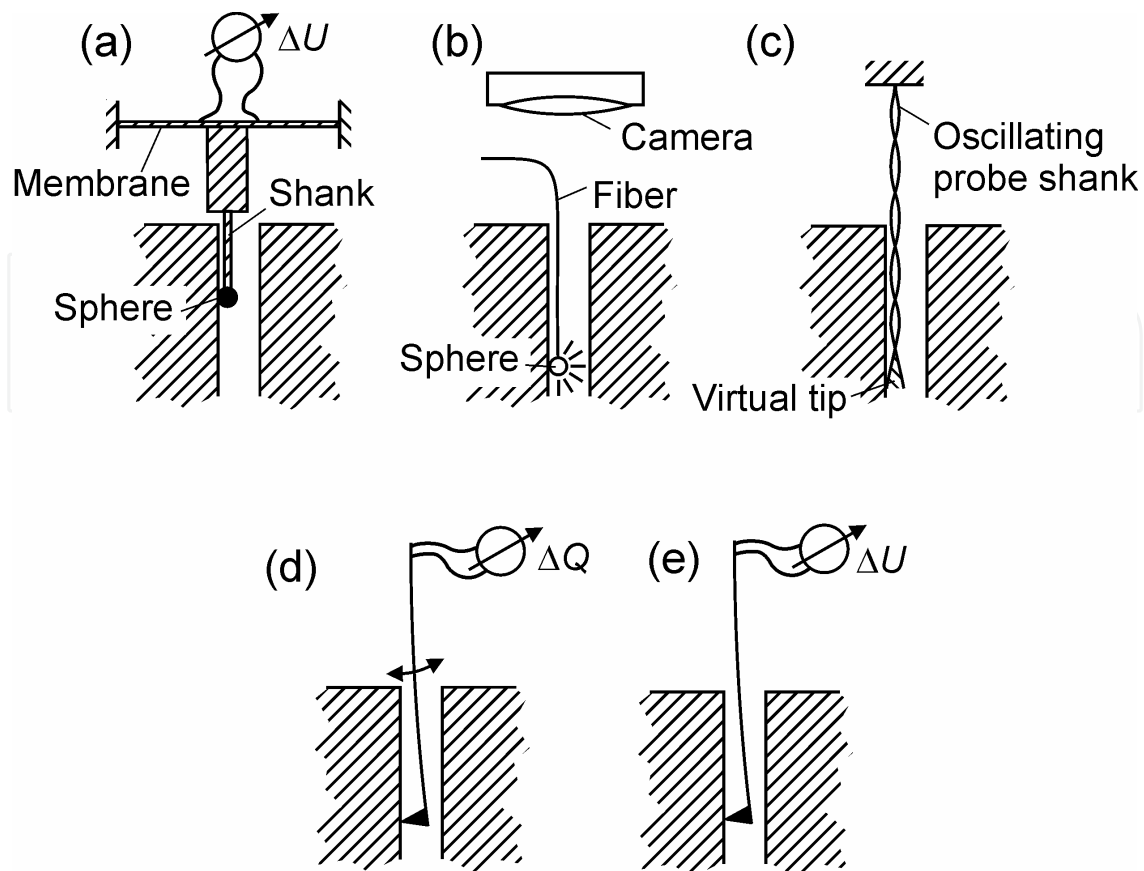


Fig. 2. Schematics of tactile probe sensors with stiff shaft (a) passive-sensing (b, c) and active-sensing (d, e) compliant shaft.

A compliant cantilever which actively senses its physical contact with a surface appears to be the most feasible concept to meet the present lack of metrology capabilities for contour and roughness measurement inside deep, narrow holes (Figs. 2d and e). Both, cantilevers using piezoelectric and piezoresistive signal transduction have been proposed in recent years (Behrens et al., 2003; Lebrasseur et al., 2002; Peiner et al., 2004; Peiner et al., 2007; Peiner et al., 2008; Pourciel et al., 2003; Yamamoto et al., 2000). Piezoelectric cantilevers of very small shaft diameter were fabricated from tungsten carbide with an integrated PZT layer for piezoelectric read-out (Yamamoto et al., 2000). However, its accuracy is limited ( $\sim 0.1 \mu\text{m}$ ) and electro discharge machining (EDM) is needed to realize the shaft.

The potential of cost-effective batch processing using bulk micromachining is provided by silicon cantilevers with piezoresistive read-out (Fig. 2e). They can be operated in both static and dynamic modes for surface scanning either at high speed or at low contact force. Furthermore, piezoresistive cantilevers can be miniaturized and integrated in an array for parallel probing applications (Choudhury et al., 2007; Mathieu et al. 2007). A first prototype of a high-aspect-ratio piezoresistive cantilever was developed and tested for inner-surface profiling of micro holes of  $80 \mu\text{m}$  in diameter and  $200 \mu\text{m}$  in depth showing an uncertainty of  $\sim 35 \text{ nm}$  (Lebrasseur et al., 2002; Pourciel et al., 2003). Tiny tips of height and radius of curvature of  $7.2 \mu\text{m}$  and less than  $50 \text{ nm}$ , respectively, were described, which are likely to be prone to damage or wear, especially during high-speed operation. Furthermore, larger tip heights are required to get access to undercut or concave surface profiles without needing a tilt of the cantilever (Pourciel et al., 2003).

Parameter	Glass / carbon fiber probe	Cantilever probe	
		Tungsten carbide	Silicon
Shaft length	2 – 200 mm	1 mm	1 – 5 mm
Shaft diameter	7 – 300 $\mu\text{m}$	10 $\mu\text{m}$ (min.)	20 – 200 $\mu\text{m}$
Probing element	glass sphere, virtual tip	integrated tip, radius 0.5 – 2 $\mu\text{m}$	integrated tip, radius 0.5 – 2 $\mu\text{m}$
Probing force	$\leq 1 \mu\text{N}$	$< 50 \mu\text{N}$	1 – 100 $\mu\text{N}$
Stiffness	few N/m	500 N/m	1 – 10 N/m
Read out	camera / piezoelectric vibration damping	piezoelectric	piezoresistive
Fabrication	piecewise	batch + piecewise	batch
Uncertainty/Repeatability	0.01 - 0.5 $\mu\text{m}$	0.1 $\mu\text{m}$	$\pm 35 \text{ nm}$
Probing speed	few tens of pts/s or few tens of $\mu\text{m/s}$	-	10 – 630 $\mu\text{m/s}$

Table 1. Comparison of tactile probing sensors for contour and roughness metrology with deep, narrow holes (Bauza et al., 2005; Behrens et al., 2003; Cusanelli et al., 2007; Kao & Shih, 2007; Lebrasseur et al., 2002, Peiner et al., 2004; Peiner et al., 2007; Peiner et al., 2008; Pourciel et al., 2003; Rauh; 2005; Woody & Bauza, 2007; Yamamoto et al., 2000; UMAP, 2008).

In this chapter, tailored slender and compliant cantilevers with integrated tips are addressed which are designed for tactile probing along high-aspect-ratio microstructures, e.g. inside deep and narrow spray holes of DI fuel nozzles (Fig. 1). A full-bridge piezoresistive strain gauge is located on the cantilever designed to be read out using a standard instrumentation amplifier. In the following, design and fabrication of slender cantilever sensors are described as well as their characterization and test in form and roughness measurements with micro holes. A schematic of the probe head and the silicon sensor chip comprising the cantilever with a probing tip and a piezoresistive strain gauge as well as contact pads for wire bonding and die testing/calibration is shown in Fig. 3. Furthermore, the circuit diagram of the strain gauge resistors connected into a Wheatstone bridge is displayed as well as an integrated resistor/diode for temperature control.

## 2. Tactile sensor

### 2.1 Layout

Design and fabrication of the slender cantilever sensor was determined by the specific requirements of tactile probing within narrow and deep micro holes:

- A high degree of freedom was required for the geometrical design of the cantilever in combination with high mechanical stability. From this point of view bulk silicon wafers were preferred over silicon-on-insulator wafers (SOI) which have a fixed thickness and are costly.
- The probing tip was integrated at the cantilever's free end. A conical shape of an angle of  $60^\circ/90^\circ$  and a radius of curvature of  $2 \mu\text{m}$  is recommended for measurements of good quality surfaces according to ISO 3274. Therefore we employed anisotropic wet tip etching instead of reactive ion etching often used for sharp and tiny atomic force

microscopy (AFM) tips. Furthermore, in contrast to AFM probes we located the tip at the bottom side of the cantilever. So, robust tips of heights ranging from 10 to 200  $\mu\text{m}$  could be realized while leaving the upper chip surface for a planar integration of the strain gauge.

- The cantilever deflection was measured using a balanced Wheatstone bridge located close to the cantilever clamping. Cantilever dimensions and bridge layout are displayed in Fig. 3. The large contact pads were provided for die testing and calibration. During the back-end processing of the probe head this area was used for the deposition of glue for the fixing of the sensor to the steel finger. Electrical connection was realized via wire bonds from the small pads on the sensor chip to a flexible circuit board glued onto the steel finger.

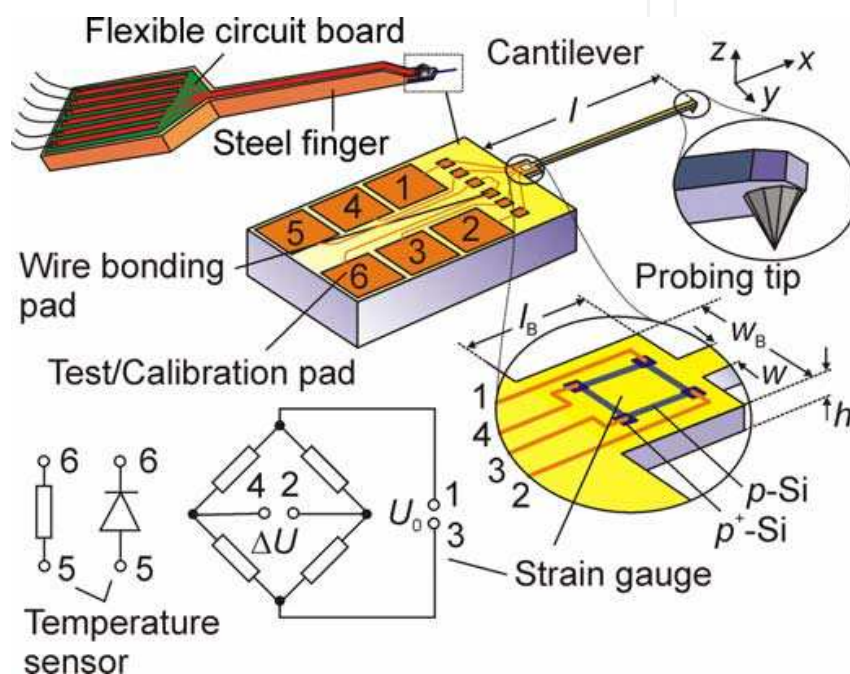


Fig. 3. Schematic of probe head based on a tactile cantilever sensor with enlarged representations of the probing tip and the Wheatstone bridge as well as the circuit diagram of the bridge and a temperature sensing device.

Slender cantilevers of low stiffness as required for probing inside narrow and deep micro holes generate only small strain values upon tip deflection. Therefore, a high gauge factor and an optimum location of the gauge on the cantilever were necessary to meet the sensitivity requirements. Simultaneously, temperature drift, susceptibility to ambient light, power consumption, and noise had to be kept as low as possible. As a trade-off we designed a full Wheatstone bridge of four *p*-type resistors of a sheet carrier concentration of  $3 \times 10^{14} \text{ cm}^{-2}$  to obtain a bridge resistance of 2.5 k $\Omega$  for which we could expect a gauge factor of  $K \approx 80$ , a temperature drift of  $\sim (1 - 2) \times 10^{-3}/\text{K}$ , noise of  $\sim 1 \mu\text{V}$  in a bandwidth of 20 kHz and a power consumption of 0.4 mW at  $U_0 = 1 \text{ V}$ .

## 2.2 Vertical loading

Using the cantilever sensor in Fig. 3 as a tactile sensor three directions of force application to the cantilever free end can be distinguished with respect to the cantilever axis: vertical, lateral and axial loading. In the case of vertical loading, i. e. the normal loading case, a

force  $F_z$  acts onto the probing tip perpendicularly to the chip plane. It results in a deflection of the cantilever of:

$$\delta_z = \frac{4l^3(1-\nu^2)}{Ewh^3} c_B F_z = \frac{1}{k} F_z \quad (1)$$

with the plate modulus  $E/(1-\nu^2) = 170$  GPa of a (001) silicon cantilever aligned to the [110] crystal direction and  $l$ ,  $w$  and  $h$  as defined in Fig. 3. Plane strain is assumed. The cantilever stiffness is denoted by  $k_z$ . The widening of the cantilever at its clamped end ( $w_B$ ,  $l_B$  cf. Fig. 3) is taken into account by the factor

$$c_B = 1 - \frac{3l_B(l-l_B)}{l^2} \left( 1 - \frac{w}{w_B} \right). \quad (2)$$

At the cantilever surface uniaxial strain is generated along the cantilever axis depending on the tip deflection  $\delta_z$ , which has its maximum at the cantilever clamping amounting to:

$$\varepsilon_B = \frac{3h}{2l^2} \frac{w}{w_B c_B} \times \delta_z \quad (3)$$

Stiffness and strain values calculated for the given cantilever geometries ( $l = 1.5 - 5$  mm,  $w = 30 - 200$   $\mu\text{m}$ ,  $h = 25 - 50$   $\mu\text{m}$ ,  $w_B = 100 - 200$   $\mu\text{m}$ ,  $l_B = 250$   $\mu\text{m}$ ) using eqs. (1) to (3) were compared with the data obtained by finite element modelling (FEM) using ANSYS 8.1. We found an agreement within 2-3 % for the stiffness and 8-10 % for the strain.

Four resistors  $R_{ij}$  (indices denote the numbers assigned to each resistor contact) are connected into a full Wheatstone bridge (Fig. 3). Assuming for simplicity that each of the four legs of the bridge, which are aligned either in parallel (longitudinal:  $R_{14}$  and  $R_{23}$ ) or perpendicularly (transversal:  $R_{12}$  and  $R_{34}$ ) to the cantilever, is uniformly strained by  $\varepsilon_B$  we observe resistance changes of almost identical absolute value but opposite sign. At a constant voltage supply to the bridge of  $U_0$  we find:

$$\frac{\Delta U}{U_0} = K \varepsilon_B \quad (4)$$

with the piezoresistive gauge factor  $K$ . Either an additional resistor or a diode is integrated close to the strain-sensing Wheatstone bridge and can be connected via the contacts 5 and 6 for on-chip temperature sensing.

### 2.3 Lateral loading

In general, during scanning over a not ideally flat work piece surface the cantilever may be deflected not only in vertical but also in lateral direction, i.e. the probing force acting on the tip is a superposition of vertical and lateral contributions. A lateral force  $F_y$  applied to the tip caused e.g. by friction forces emerging during scanning the cantilever over a surface in the direction perpendicular to the cantilever axis lead to a lateral cantilever deflection. Simultaneously, a moment about the cantilever axis is exerted causing an additional tip deflection. In total we obtain:

$$\delta_y = \left[ \frac{4l^3(1-\nu^2)}{Ehw^3} + c_{\text{torsion}} \frac{(h_t + h/2)^2 l}{Gwh^3} \right] F_y = \frac{1}{k_y} F_y \quad (5)$$

with the shear modulus  $G = E/(1 + \nu) = 80 \text{ GPa}$  ( $\nu = 0.064$ ) and  $c_{\text{torsion}} = 3.6$  for  $h/w = 4$  and  $c_{\text{torsion}} = 7.1$  for  $h/w = 1$  (Bao 2000). In the present case of slender cantilevers, i. e.  $h \cdot w \cdot 0.02l$  and a tip height of  $h_t \# h$  the torsional contribution is more than two orders of magnitude smaller than the lateral bending. This was confirmed by FEM. Non-uniform uniaxial strain across the Wheatstone bridge is induced: At a lateral deflection  $\delta_y$  the longitudinally oriented resistors ( $R_{14}$  and  $R_{23}$ ) are strained at equal absolute value but at opposite sign

$$\varepsilon_B = \frac{3w}{4l^2} \times \delta_y$$

while strain across the transversally oriented resistors ( $R_{12}$  and  $R_{34}$ ) averages to zero. The longitudinal resistors are located at  $\pm w/2$  from the neutral axis. Connecting both longitudinal resistors into a half bridge (hb) we obtain an output signal of:

$$\left( \frac{\Delta U}{U_0} \right)_{\text{hb}} = \frac{1}{2} K \frac{3w}{4l^2} \times \delta_y \quad (6)$$

## 2.4 Axial loading

Axial loading results from moving the cantilever with its free end against a fixed body. Three modes of deflection of an axially loaded cantilever which have been implemented in MEMS technology (Beyeler et al., 2008; Ruther et al. 2007; Samuel et al., 2006) are schematically shown in Fig. 4 where cantilevers fixed to a support by clamping (left), a hinge (middle) and a spring (right) are depicted. Due to its slender shape the first one is best suited for probing the bottom surface of deep and narrow blind holes, e.g. through silicon vias (TSV) for 3D interconnects. Under an axial load  $F_x$  a cantilever beam is uniformly compressed until buckling occurs, when  $F_x$  exceeds a critical value:

$$F_c = \beta \left( \frac{\pi}{l} \right)^2 \frac{Ewh^3}{12} \quad (7)$$

In this case a uniform rectangular cross section was assumed. The constant  $\beta$  depends on the boundary conditions, i. e.  $\beta = 1/4$  for a beam with one end clamped and the other free (type I) and  $\beta = 1/(0.7)^2$  for a beam with one end clamped and the other pinned (type II). In the case of slight initial cantilever bending buckling occurs gradually as the load approaches  $F_c$ . Below  $F_c$  the cantilever is uniformly compressed leading to a strain at the piezoresistive bridge of:

$$\varepsilon_B = \frac{k_x}{Ewh} \times \delta_x \quad (8)$$

with the axial stiffness of the cantilever:

$$k_x = \frac{Ewh}{l} \quad (9)$$

For a 5-mm-long cantilever and a gauge factor of the piezoresistive bridge of 80 we find a sensitivity of 16 mV/ $\mu\text{m}$ .

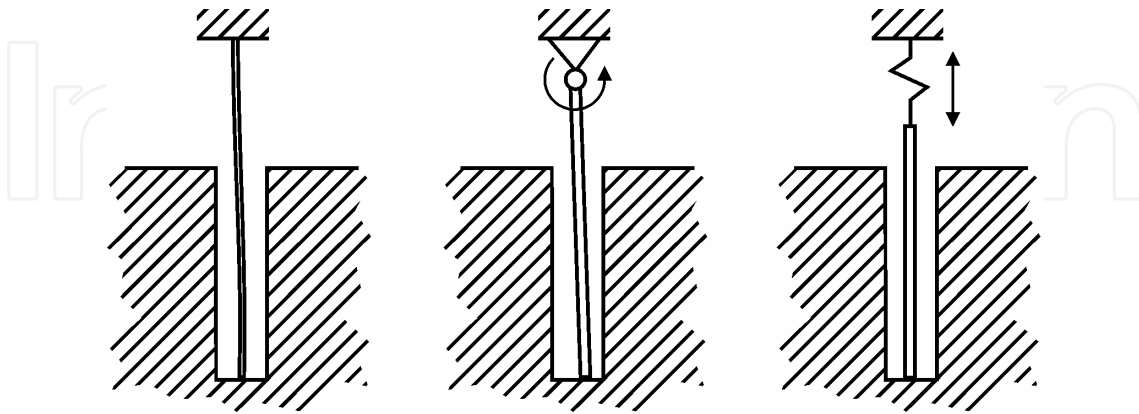


Fig. 4. Schematic of tactile sensing using axially loaded cantilevers.

## 2.5 Fabrication

Sensor prototypes were realized using a bulk micromachining process which is schematically shown with a sectioned piece of the silicon chip in Fig. 5:

- An *n*-doped (100) silicon wafer ( $300 \pm 3 \mu\text{m}$ ) was thinned in a time-controlled process using either deep reactive ion etching (DRIE,  $\text{SF}_6/\text{O}_2$ ) at cryogenic temperature ( $75^\circ\text{C}$  to  $-95^\circ\text{C}$ ) or wet anisotropic etching in TMAH (tetra methyl ammonium hydroxide, 20 %,  $80^\circ\text{C}$ ) solution through a mask of photo resist or thermal oxide, respectively. Etching was stopped at a residual thickness corresponding to the desired cantilever thickness plus the tip height (Fig. 5a). The standard deviation of the thickness measured with the generated membranes was typically less than 1 %. An advantage of cryogenic DRIE over anisotropic wet etching is the considerably higher etch rate of  $\sim 4 \mu\text{m}/\text{min}$  vs.  $0.7 \mu\text{m}$  for TMAH. Thus, the time consumed for this process step is drastically reduced from  $\sim 6$  h to  $\sim 1$  h. Furthermore, a photo resist mask can be employed instead of thermal oxide needed for TMAH etching.
- Subsequently, *p*-type stripes arranged in a square geometry were designed as the resistor legs of a full Wheatstone bridge (Fig. 5a). They were realized by boron diffusion from a spin-on silica emulsion source (Emulsitone Borofilm 100) or by boron implantation. Contact formation to the *p*-type silicon was improved by an extra boron diffusion/implantation dose in the corner regions of the bridge square (Fig. 5b). The standard deviation of the measured resistivity about the target value was 4.1 % and 0.6 % for the diffused and implanted wafers, respectively. The doping profile was measured during various stages of the process with monitor wafers using electrochemical capacitance-voltage profiling (ECV). Subsequent to the final high-temperature step we found a junction depth of  $4.5 \mu\text{m}$  and a surface concentration of  $1.5\text{-}3.0 \times 10^{18} \text{ cm}^{-3}$  which is a tradeoff to obtain a high piezoresistive coefficient around  $\pi_{44} \approx 1 \text{ GPa}^{-1}$  and a low temperature coefficient around  $1 \times 10^{-3} \text{ K}^{-1}$  (Cho et al., 2006).
- A probing tip was generated at the cantilever bottom side by undercut etching of a circular or square oxide (nitride) mask using either TMAH or KOH (Fig. 5c). In this case

photolithography had to be performed within the backside-etched depression shown in Figs. 5a and b. Its depth was determined by the desired tip height, i.e., it has a maximum value of  $\sim 250 \mu\text{m}$  for the smallest tips. Using single exposure of positive resist (Shipley, S1818) we realized squares of an edge length of  $\sim 70 \mu\text{m}$  as the smallest structures showing deviations from the desired length of typically less than 10%. During anisotropic etching a micro pyramid with an octagonal base developed underneath the mask with its angle of apex determined by the emerging sidewall facets. We used TMAH (20%, 80 °C) and KOH (45%, 80 °C) to generate tip angles of  $\sim 90^\circ$  and  $\sim 40^\circ$ , respectively. SEM photographs of tips in the backside-etched groove before and just after complete under etching of a square oxide mask using KOH (45%, 80 °C) are depicted in Figs. 6a and b, respectively.

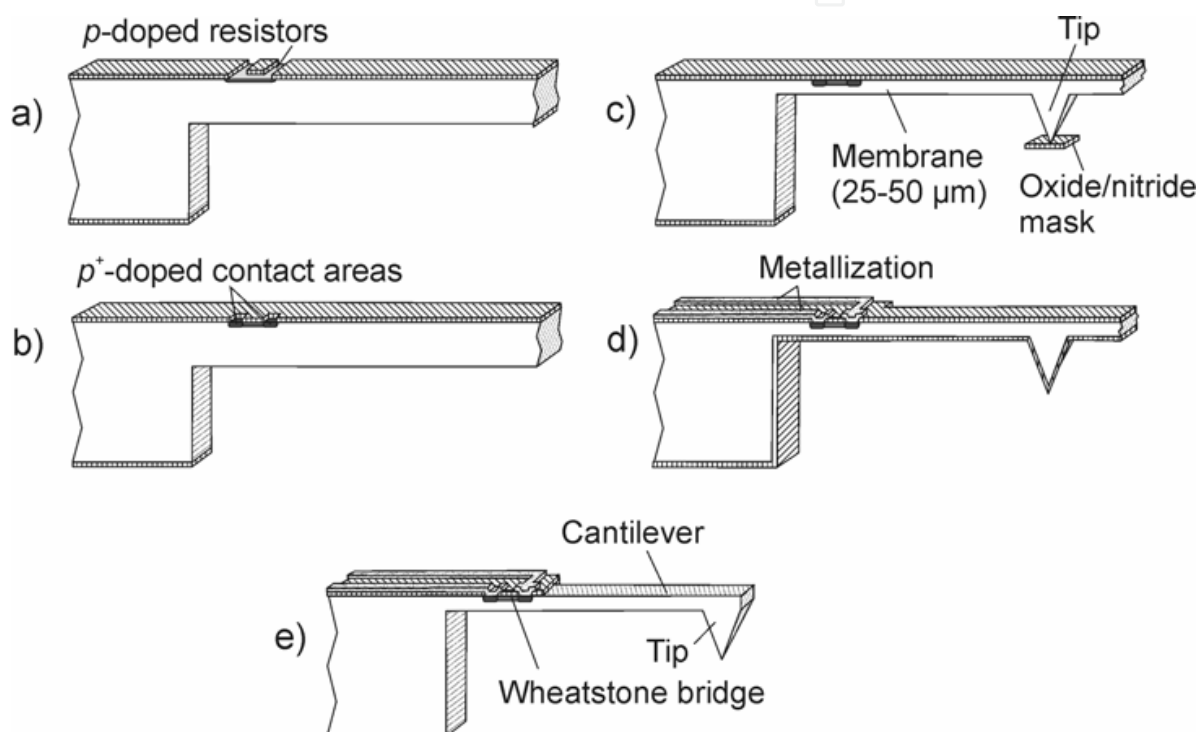


Fig. 5. Schematic of the sensor fabrication process: Membrane etching (a), boron doping (a, b), tip etching (c), metallization (d) and cantilever etching (e).

- After tip formation the wafer was oxidized and patterned for contact holes to the Wheatstone bridge. Either a gold/chromium or an aluminum metallization was used (Fig. 5d).
- Finally, the cantilever was released by either DRIE at cryogenic temperatures using  $\text{SF}_6/\text{O}_2$  or anisotropic wet etching using KOH (30%, 60 °C) (Fig. 5e). In both cases a protection of the Au/Cr metallization was not necessary. In the case of DRIE we could employ a photo resist mask and a CMOS compatible Al metallization while an oxide mask and an Au/Cr metallization were used for the KOH process. Samples of the cantilever sensor of 1.5-5 mm in length, 30-200  $\mu\text{m}$  in width and 25-50  $\mu\text{m}$  in height are shown in Fig. 7.

Figure 8 shows a realized probe head comprising the cantilever sensor mounted on a steal finger, a retractable plastic cover protecting the cantilever during transport and mounting bracket.

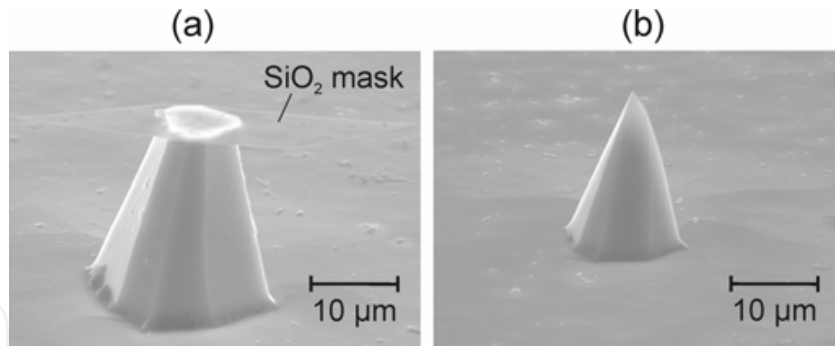


Fig. 6. SEM photographs of tips in the backside-etched groove before (a) and just after complete under etching (b) of a square oxide mask using KOH (45 %, 80 °C).

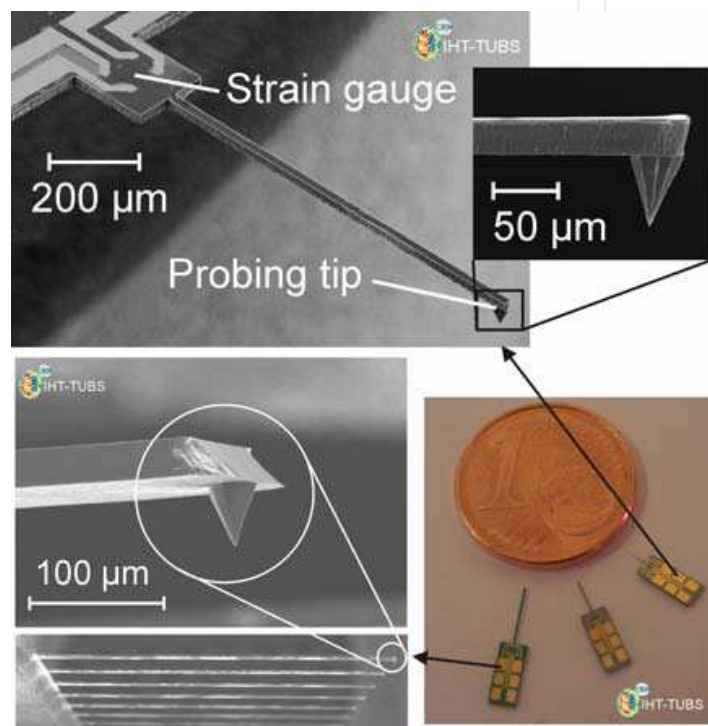


Fig. 7. Samples of slender piezoresistive cantilever sensors with integrated probing tip. Either DRIE at cryogenic temperatures (upper) or wet etching using KOH (lower) was employed for the final release of the cantilevers.

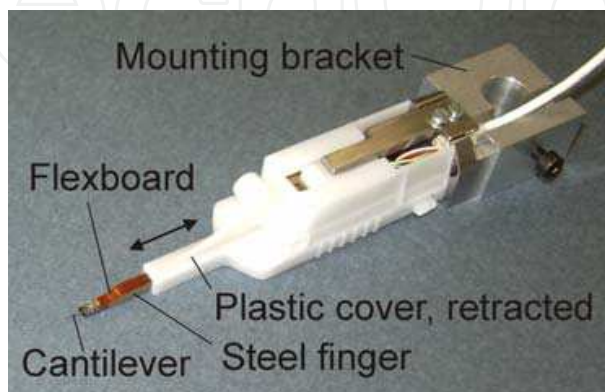


Fig. 8. Probe head after back-end processing. A plastic cover serving as a protection of the cantilever during transport and mounting into a scanning unit is retracted.

### 3. Sensor performance

Realized sensors were calibrated using a nanonewton force testing setup (Behrens et al., 2003; Peiner et al., 2007; Peiner et al., 2008). For this purpose the sensor dies were mounted into a custom-made metal case. Electrical connection was provided using contact pins which were pressed against the large contact pads shown in Fig. 3 serving as the counterparts for a temporary, easily detachable connection. Temperature and relative humidity in the calibration box were stabilized within 21.4 - 23.5 °C and 23 - 39 %, respectively. The output signal of the full Wheatstone bridge operated at a supply voltage of  $U_0 = 1$  V was connected to an instrumentation amplifier (HBM, ML 10B) via a shielded cable. During a typical calibration measurement the cantilever was incrementally moved with its tip against the weighing pan of an electronic balance (Sartorius, SC 2). Simultaneously with the force measurement the output signal  $\Delta U$  of the integrated piezoresistive gauge was recorded. A calibration curve typically comprised  $\sim 100$  sample increments and was repeated  $\sim 500 \times$  for each sensor device.

The complete setup was mounted on a platform comprising stabilizer pneumatic isolators with automatic leveling for vibration damping to cancel ground vibrations and acoustic noise. A shielded cable was used to protect the bridge output signal against electromagnetic interference.

#### 3.1 Vertical loading

The typically measured performance data of realized 5-mm-long silicon cantilever sensors were listed in Table 2. Cantilevers show linear load-deflection characteristics in a range up to 200  $\mu\text{m}$  with a fracture limit exceeding 1.6 mm. For the stiffness we found  $\sim 12$  N/m at a repeatability of 2.5 %. The stiffness of the balance of  $> 10$  kN/m is by far higher. Therefore, it was not taken into account for the analysis of the cantilever stiffness. The main source for a deviation from the design value was the cantilever height given by the etching in a time-controlled process. Measurements across the wafer showed a typical variation of  $\sim 1 - 2$  % about the target height.

Parameter	Value
Range $\delta_{\max}$	200 $\mu\text{m}$ @ FS, fracture limit: $\delta_z > 1.6$ mm, $\delta_y > 0.3$ mm
Stiffness	11.9 N/m @ repeatability of 2.5 %
Sensitivity $S$	0.25 $\mu\text{V}/\text{nm}$ @ without amplification, repeatability of 1 %
Non-linearity	0.3 %FS @ 200 $\mu\text{m}$ , 0.2 %FS @ 20 $\mu\text{m}$
Gauge factor $K$	$76 \pm 2$
Switch-on delay	$\sim 1$ s
Temperature coefficient of $R$	- 0.2 %/K
Temperature drift	10 nm/K @ referred to vertical deflection
Light sensitivity	4-10 nm @ neon light: 100 $\mu\text{W}/\text{cm}^2$ , referred to vertical deflection
Long-term stability	6 nm @ 70 h, $\Delta T < 1$ K, referred to vertical deflection
Resolution $\delta_{\min}$	1.8 nm @ $f_{\max} = 1.6$ kHz, $f_{\min} = 0.003$ Hz 1.3 nm @ $f_{\max} = 800$ Hz, $f_{\min} = 0.003$ Hz 0.6 nm @ $f_{\max} = 100$ Hz, $f_{\min} = 0.003$ Hz
Uncertainty ( $k = 2$ )	30 nm @ 1 $\mu\text{m}$

Table 2. Sensor performance ( $l = 5$  mm,  $w = 200$   $\mu\text{m}$ ,  $h = 50$   $\mu\text{m}$ ,  $U_0 = 1$  V,  $T = 21.4 - 23.5$  °C,  $rH = 23 - 39$  %.)

A deflection sensitivity of  $0.25 \mu\text{V}/\text{nm}$  and a non-linearity of  $0.3 \%$ FS was measured at a repeatability of  $1 \%$  in an exceptionally large deflection range up to  $200 \mu\text{m}$ . Using eqs. (3) and (4) we could calculate from these results a gauge factor of  $K = 76 \pm 2$  which is close to the desired value of 80. The resistivity showed a temperature coefficient of  $-0.2 \%/K$ . A stable read-out signal was achieved typically within one second after switch-on of the voltage supply. The cross sensitivity against temperature and ambient light was below  $10 \text{ nm}$  at  $\Delta T = 1 \text{ K}$  and an illumination intensity of  $100 \mu\text{W}/\text{cm}^2$ , respectively. The input-referred stability of the strain-gauge output signal amounted to  $6 \text{ nm}$  over  $70 \text{ h}$  at  $\Delta T < 1 \text{ K}$ . Noise of the complete system including sensor and amplifier measured in a frequency range from  $10^{-3} \text{ Hz}$  to  $20 \text{ kHz}$  showed characteristic  $1/f$  and white noise regimes below and above  $\sim 10 \text{ Hz}$ , respectively (Peiner et al., 2007). White noise of  $5.8 \times 10^{-11} \text{ mV}^2/\text{Hz}$  can be calculated for a symmetric Wheatstone bridge of a resistance of  $2.5 \text{ k}\Omega$  of each leg. This corresponds very well to the measured value of  $6 \times 10^{-11} \text{ mV}^2/\text{Hz}$  obtained as the difference of measured total and amplifier noise in the white noise regime.  $1/f$  noise comprises contributions from both the Wheatstone bridge and the amplifier according to:

$$\frac{\overline{U_H^2}}{f} = \left( \frac{\alpha U_0^2}{2N} + \overline{U_A^2} \right) / f \quad (10)$$

where  $\alpha$ ,  $N$  and  $\overline{U_A^2}$  denote the Hooge constant, the total number of carriers in a single resistor, and the amplifier noise, respectively (Nesterov & Brand, 2006). With the bridge supply voltage of  $1 \text{ V}$  and a total number of carriers of  $2.5 \times 10^9$  within each resistor we calculate a Hooge constant of  $\alpha = 1.3 \times 10^{-6}$ .

Integration of  $1/f$  noise and white noise (Johnson noise:  $\overline{U_J^2} / \Delta f$ ) from  $f_1$  to  $f_2$  yields:

$$\overline{U_{\text{noise}}^2} = \overline{U_H^2} \ln \left( \frac{f_2}{f_1} \right) + \frac{\overline{U_J^2}}{\Delta f} (f_2 - f_1) \quad (11)$$

With  $\overline{U_H^2} = 8 \times 10^{-10} (\text{mV})^2$ ,  $\overline{U_J^2} / \Delta f = 1.5 \times 10^{-10} (\text{mV})^2 / \text{Hz}$ ,  $f_1 = 10^{-3} \text{ Hz}$  and  $f_2 = 1.6 \text{ kHz}$  we find  $\sqrt{\overline{U_{\text{noise}}^2}} = 0.5 \mu\text{V}$ , which at a sensitivity of  $0.25 \mu\text{V}/\text{nm}$  corresponds to a resolution of  $2 \text{ nm}$ .

A high sampling rate is required for scanning at high levels of speed ( $> 1 \text{ mm}/\text{s}$ ) and lateral resolution ( $< 1 \mu\text{m}$ ), i.e. the ratio of scanning speed to upper cutoff frequency should be on one hand considerably lower than the minimum lateral structure width which has to be resolved. On the other hand, however, for nanometer vertical resolution high-frequency noise has to be cancelled by reducing the upper cutoff frequency. As a tradeoff we selected an upper cutoff frequency of  $100 \text{ Hz}$  and reduced the probing speed to around  $10 \mu\text{m}/\text{s}$ , if nanometer vertical resolution and sub-micrometer lateral resolution were required. If a lower vertical resolution around  $10 \text{ nm}$  was acceptable we could operate the amplifier at  $19.2 \text{ kHz}$  and increase the probing speed to around  $1 \text{ mm}/\text{s}$ .

We tested the vertical and lateral scanning resolution using a photolithography mask comprising  $60\text{-nm}$ -high and  $1\text{-to-}10\text{-}\mu\text{m}$ -wide stripes of chromium on a glass substrate. Scanning of the entire test area of  $310 - 100 \mu\text{m}^2$  in the fast modus, i.e. within  $< 3 \text{ min}$  reveals all stripes clearly resolved. High-resolution scans were then performed with the 1-, 2-, and

3- $\mu\text{m}$ -wide stripes at a speed of 15  $\mu\text{m}/\text{s}$  and an upper cutoff frequency of 100 Hz. According to the noise analysis we can expect lateral and vertical resolutions of 0.15  $\mu\text{m}$  and 0.5 nm, respectively. Measured stripe heights and widths are summarized in Table 3 showing deviations from the nominal height and width of less than 16 % and 6 %, respectively. The measured stripe width corresponds to the distance between the raising and falling flanks at 90 % of the height. The variances measured for the heights of 1.6 to 2.5 nm are higher than expected. They can be assigned to a 50 Hz interference due to not perfect shielding of the signal transmission. Measurement uncertainty was determined within the deflection range of 0.3 - 10  $\mu\text{m}$  using a depth setting standard (EN 48200). We found a value of 30 nm ( $k = 2$ ) for a deflection of 1  $\mu\text{m}$ . These results confirm the potential of the described slender piezoresistive cantilever sensor for contour and roughness measurements of structured surfaces at sub-micron lateral and nanometer vertical resolutions.

nominal stripe width ( $\mu\text{m}$ )	measured stripe width ( $\mu\text{m}$ )	measured stripe height (nm)
1	$1.06 \pm 0.01$	$51.8 \pm 1.9$
2	$1.96 \pm 0.01$	$53.2 \pm 2.5$
3	$3.03 \pm 0.01$	$50.7 \pm 1.6$

Table 3. Scanning across Cr stripes on a glass carrier using a slender cantilever sensor ( $l = 3 \text{ mm}$ ,  $w = 100 \mu\text{m}$ ,  $w = 50 \mu\text{m}$ ,  $U_0 = 1\text{V}$ , scanning speed = 15  $\mu\text{m}/\text{s}$ , probing force = 80  $\mu\text{N}$ ,  $f_2 = 100 \text{ Hz}$ ).

### 3.2 Lateral loading

We investigated the behaviour of a cantilever of uniform cross section of  $l = 5 \text{ mm}$ ,  $w = 200 \mu\text{m}$ , and  $h = 40 \mu\text{m}$  under combined vertical and lateral loading. Combining eqs. (4) and (6) we find a ratio of lateral-to-vertical sensitivity of  $w/(4h) = 1.25$ . Measurements were performed of the output signals of the strain gauge resistors under tilted loading conditions, i.e. by moving the tip against a flat work piece inclined by  $-30^\circ$  and  $45^\circ$  about an axis parallel to the cantilever axis. We find values of 0.84-0.93 for the ratio of lateral-to-vertical sensitivity which in fair agreement with the expected value of 1.25. Thus, vertical and lateral signals can be decoupled by analyzing the responses of all four resistors in the conventional full bridge arrangement and the longitudinal resistors alone connected into a half bridge, respectively.

### 3.3 Axial loading

Moving a cantilever with its free end axially against a fixed body can lead to three different stages of deformation as schematically displayed in Fig. 9a. Initially, it is uniformly compressed. After exceeding a critical load  $F_c$  (eq. (7)) buckling occurs which may be either of type I or II depending on whether the cantilever free end can move or is pinned on the probed surface. Axial loading tests were performed with cantilever sensors below and above the critical load for buckling  $F_c$ . The photographs in Fig. 9b to d show an axially loaded 5-mm-long cantilever at the initial surface contact (b) and at axial displacements of  $\delta_x = 2 \mu\text{m}$  and  $\delta_x = 80 \mu\text{m}$ , respectively. In Fig. 9d the type-II buckling form of a beam is exhibited which typically occurs under the boundary conditions of the cantilever of one end clamped and the other pinned.

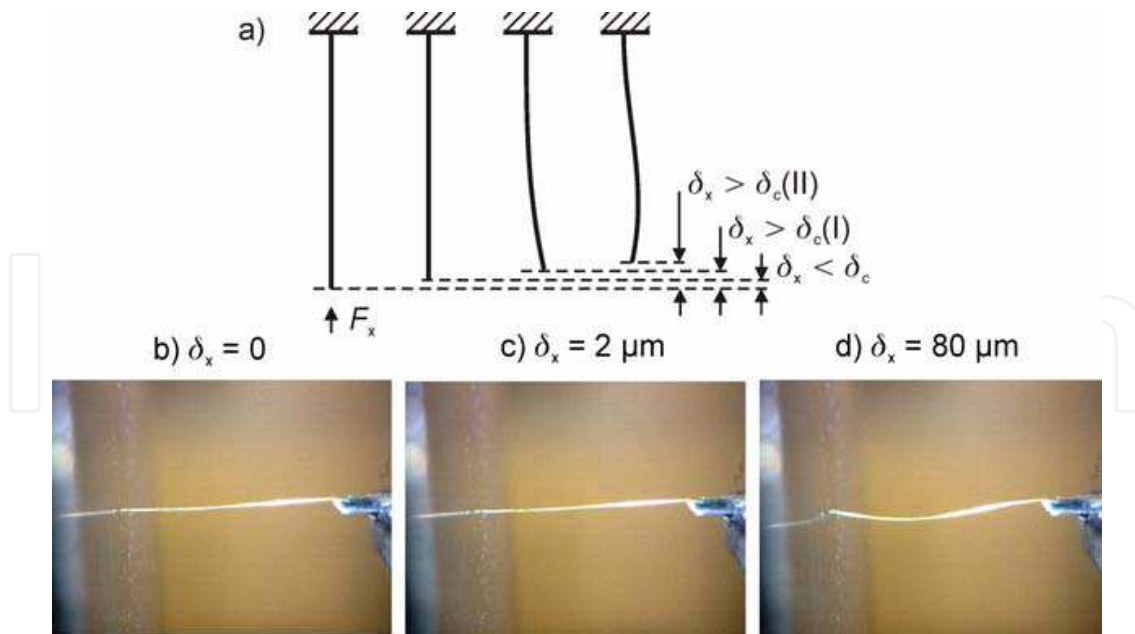


Fig. 9. Schematic (a) and photographs of an axially loaded 5-mm-long cantilever (b-d) at different stages of axial displacement.

The sensor response measured with the cantilever depicted in Figs. 9b-d during axial loading is shown in Fig. 10a where the sensor signal is displayed in dependence on the axial displacement of the cantilever moved against a fixed body. Two probing speeds were selected: 0.25 and 8  $\mu\text{m/s}$ . Up to a maximum displacement of 40  $\mu\text{m}$  an almost linear increase of the output signal amplitude with  $\delta_x$  is observed at 0.25  $\mu\text{m/s}$  with a buckling form of type I (Fig. 9b). At  $\delta_x = 50 \mu\text{m}$  the signal drastically increased corresponding to the transition from type-I to type-II buckling (Fig. 9d). At a probing speed of 8  $\mu\text{m/s}$  this transition occurred much earlier, i. e. at an axial displacement between 10 and 20  $\mu\text{m}$  indicating the dynamic-loading effect. The sensitivities of  $\sim 0.5 \text{ mV}/\mu\text{m}$  and  $\sim 4 \text{ mV}/\mu\text{m}$  observed under the conditions of type-I and type-II buckling, respectively, are lower than the sensitivity of 16  $\text{mV}/\mu\text{m}$  expected for uniform compression.

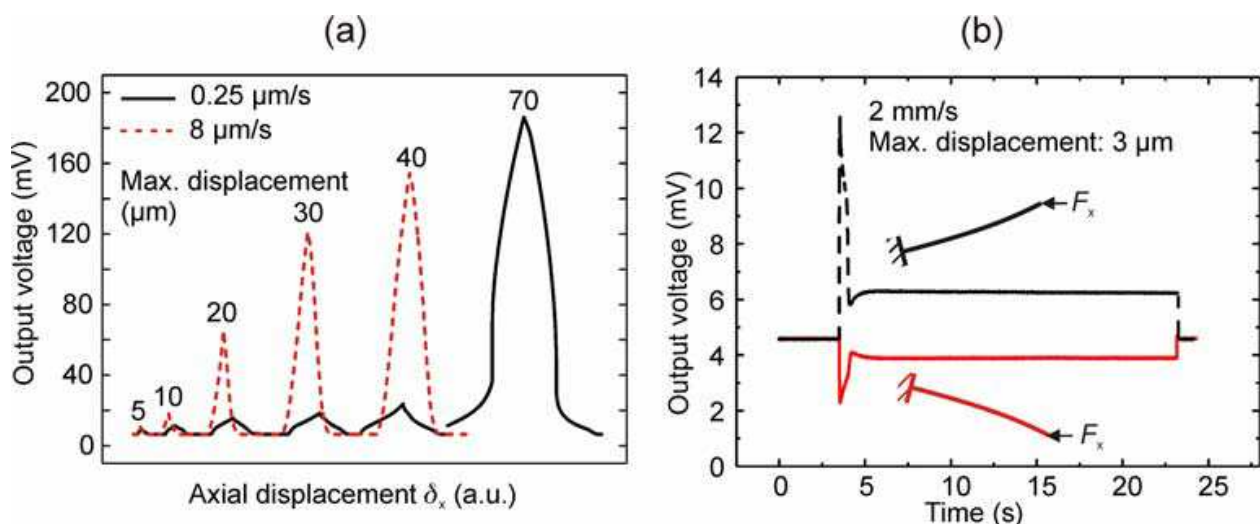


Fig. 10. Signal of an axially loaded 5-mm-long cantilever at different levels of maximum displacement (a) and at high-speed loading at inclination angles of  $\pm 15^\circ$  (b)

In Fig. 10b the sensor response on high-speed axial probing (2 mm/s) against a fixed body at a maximum displacement of 3  $\mu\text{m}$  and an inclination angle of  $\pm 15^\circ$  is shown. Type-I buckling is observed in both cases with positive and negative signs of signal change indicating compressive and tensile strain, respectively, to the Wheatstone bridge. After an initial sharp increase the signals rapidly decayed towards constant amplitudes.

Finally, axial loading tests below  $F_c$  were performed using the nanonewton force testing setup described above. Under these conditions the balance stiffness is much less than the axial cantilever stiffness  $k_x$  calculated using the cantilever dimensions and eq. (9). We find values of typically  $> 100$  kN/m. Therefore, the balance stiffness had to be considered when the measured load-deflection curves were analyzed.

Parameter	Value
Vertical sensitivity $S_z$	$0.1953 \pm 0.0008 \mu\text{V}/\text{nm}$ @ without amplification
Axial sensitivity $S_x$	$11.15 \mu\text{V}/\text{nm}$ @ without amplification $8.5 \mu\text{V}/\text{nm}$ @ calculated using eqs. (4) and (8)
Average residual from linearity	$\pm 5 \mu\text{V}$ @ 0.7 mV FS
Stiffness $k_z$	$16.33 \pm 0.04$ N/m
Stiffness $k_x$	$261.6$ kN/m @ calculated using eq. (9)
Axial deflection before buckling	$1.2 \mu\text{m}$ @ calculated using $k_x$ and eq. (8)
Fracture limit	$580 \pm 58 \mu\text{m}$ @ vertical deflection $300 \pm 30 \mu\text{m}$ @ lateral deflection $260 \pm 26 \mu\text{m}$ @ axial deflection

Table 4. Sensor performance ( $l = 3$  mm,  $w = 100 \mu\text{m}$ ,  $U_0 = 1\text{V}$ ,  $T = 22.0 - 22.1^\circ\text{C}$ ,  $rH = 40.1 - 41.5\%$ .)

In Table 4 the results obtained from the calibration of a slender cantilever sensor are summarized. Vertical stiffness  $k_z$  and sensitivity  $S_z$  were measured and analyzed using eqs. (1) to (5) yielding a cantilever thickness of  $h = 46.2 \mu\text{m}$  and a gauge factor of  $K = 25.4$ . Under axial loading we observed a stiffness of  $11.46$  kN/m which is much less than the axial cantilever stiffness  $k_x = 261.6$  kN/m calculated using eq. (9), i. e. it nearly corresponds to the balance stiffness. For the axial sensitivity we measured a value of  $0.488 \mu\text{V}/\text{nm}$  which had to be corrected by multiplying with the ratio of measured stiffness to  $k_x$  yielding  $S_x = 11.15 \mu\text{V}/\text{nm}$ . Using eqs. (4) and (8) we obtain a axial sensitivity of  $S_x = 8.5 \mu\text{V}/\text{nm}$  which is in fair agreement with the measurement.

#### 4. Form measurement

Silicon wafers patterned by deep reactive ion etching (DRIE) and spray holes manufactured using electro discharge machining (EDM) were used as artefacts of form and roughness measurements using the described slender cantilever sensor.

##### 4.1 Micro sac hole

The results of the previous chapter show that a front-side loaded slender cantilever can be used to measure the depth of a micro sac hole. The highest sensitivity occurred at uniform compression but even at  $F > F_c$  we observed values around  $1 \mu\text{V}/\text{nm}$  leading to sub nanometer resolution. We checked the measurement uncertainty by repeatedly measuring the height  $\Delta h$  of a step fabricated on a silicon wafer using DRIE. The results are displayed in

Fig. 11 where the measured values of the step height are plotted. A typical trace of the sensor signal in dependence on axial cantilever position is shown in the inset. The contact position  $x_0$  was defined as the position where the signal exceeded the average zero signal (offset voltage) by the fivefold of its standard deviation. For the step we found a mean value of  $252.407\mu\text{m}$  at a standard deviation of  $\sigma = 82\text{ nm}$ .

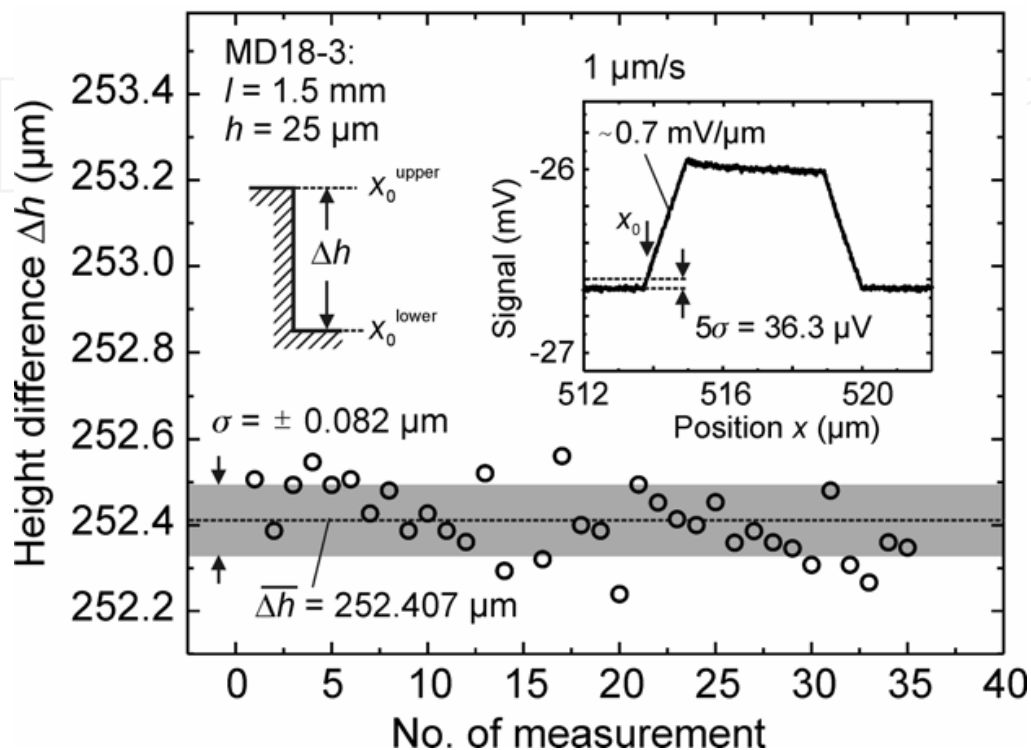


Fig. 11. Step height measured with a DRIE patterned silicon wafer using an axially loaded cantilever.

#### 4.2 Injector nozzle

VCO (valve covered orifice) direct injection (DI) Diesel nozzles with six spray holes of  $110 - 170\text{ }\mu\text{m}$  in diameter fabricated by (EDM) were investigated using realized prototype sensors to check the capability of slender piezoresistive cantilevers for in-hole form and roughness measurements. For these experiments we used  $1.5\text{-mm-long}$ ,  $30\text{-}\mu\text{m-wide}$ , and  $36\text{-to-}41\text{-}\mu\text{m}$  high cantilever sensors with  $50\text{-}\mu\text{m-high}$  tips of a radius of curvature of  $1.5\text{ }\mu\text{m}$  and a cone angle of  $40^\circ$ . Calibration of the sensors yielded a vertical sensitivity of  $\Delta U/\delta_z = 0.25 - 0.31\text{ }\mu\text{V}/\text{nm}$  and a vertical stiffness of  $k_z = 19.2 - 29.1\text{ N/m}$ .

A photograph and a schematic of the measurement setup are depicted in Fig. 12. The cantilever sensor with the piezoresistive Wheatstone bridge was connected via Au wire bonding to a printed circuit board and then via unshielded cables to an instrumentation amplifier (HBM ML 10B). This experimental probe head was then mounted on a 2D piezo positioning stage featuring a travel range of  $800\text{ }\mu\text{m}$  at sub-nanometer resolution (P-628.2CD with digital piezo controller PI 710, Physik Instrumente, Germany) which was fixed for rough positioning to an  $x$ -/ $y$ -/ $z$ -table. The nozzle was arranged on a rotating/tilting stage. Before starting the scanning process the cantilever and hole axes were carefully adjusted.

The schematic in Fig. 13 shows the movement of a cantilever sensor along the inner contour of a spray hole. Before moving into the hole the cantilever had to be carefully aligned to the

hole axis. Digital optical micrographs of a VCO nozzle and a slender cantilever into one the six spray holes are depicted in Fig. 14.

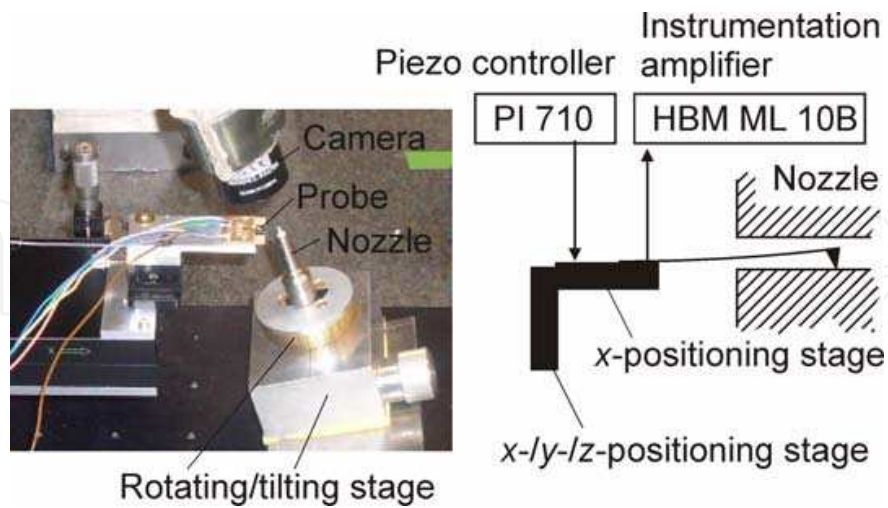


Fig. 12. Photograph (left) and schematic (right) of a setup for surface scanning inside spray holes of DI nozzles.

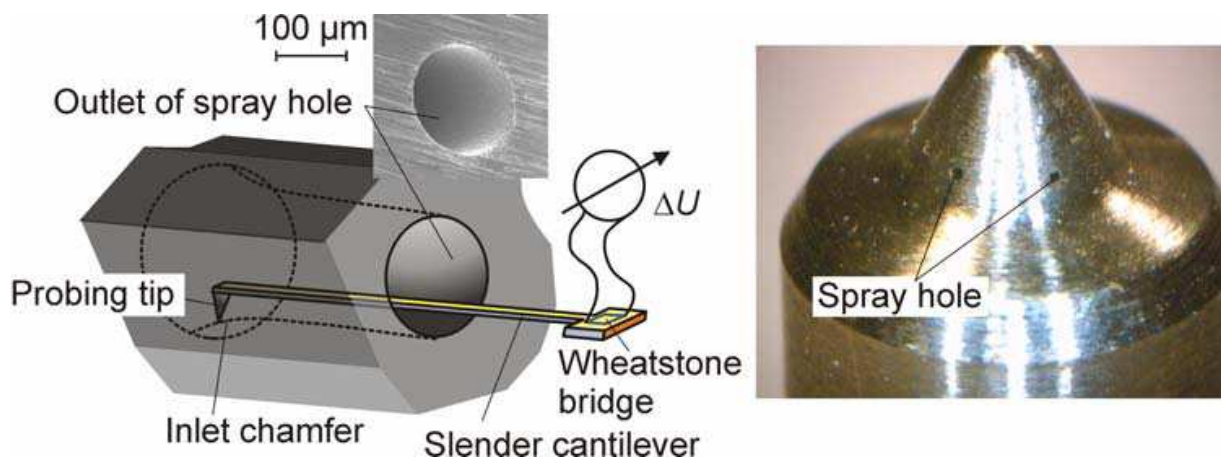


Fig. 13. Schematic of a slender cantilever sensor during scanning along the inner surface profile of deep narrow micro hole.

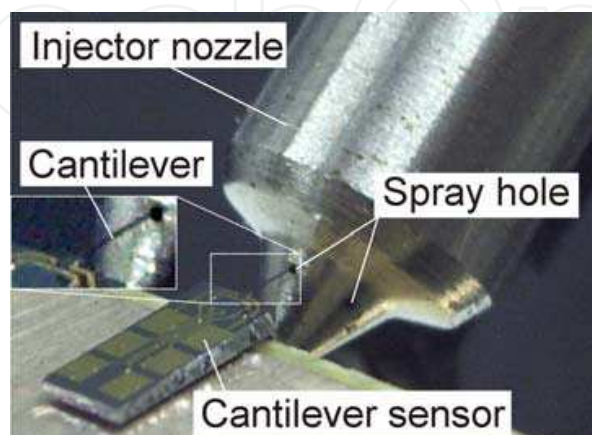


Fig. 14. Optical micrographs of a VCO Diesel injector nozzle with a slender cantilever sensor probing inside a spray hole.

Fig. 15 shows the complete inner-surface profile of the spray hole measured using a slender cantilever sensor. The scans performed at a constant speed of 2 – 200  $\mu\text{m}/\text{s}$  were started at the inner hole edge, i.e. at the entry of fuel flow. A step of 50  $\mu\text{m}$  in height corresponding to the tip height was measured during the initial scanning stage which can be assigned to the transition from shaft contact at the beginning of the scan to tip contact (outer left schematic). Then the tip touched the injector wall with its side facet and was moved along the hole edge until the hole wall was reached (inner left schematic). Linear slopes of  $30^\circ$  and  $23^\circ$  appeared at the rising and the trailing flanks, respectively, which are close to the half of the tip angle. Thus both the rising and the trailing flanks of the profiles represent superpositions of the shapes of the tip and the hole edge, respectively.

Regular probing conditions were achieved when the inlet edge of the hole was reached (inner right schematic) and the tip is moved further (outer right schematic). The profile in Fig. 15 corresponds to a not optimal form of a micro hole by EDM indicating a neck at the hole inlet. Necking is related to the loss of erosion particles occurring at the end of the drilling operation, leading to a constricted diameter of the hole at the inlet (Diver et al., 2004). For the surface roughness we found values of 0.4-0.8  $\mu\text{m}$  which is a typical range for micro holes fabricated by EDM (Li et al., 2007; Cusanelli et al., 2007; Diver et al., 2004). Abrasive flow machining (AFM) can be used subsequent to the EDM process to improve surface finish and chamfer radius (Jung et al., 2008).

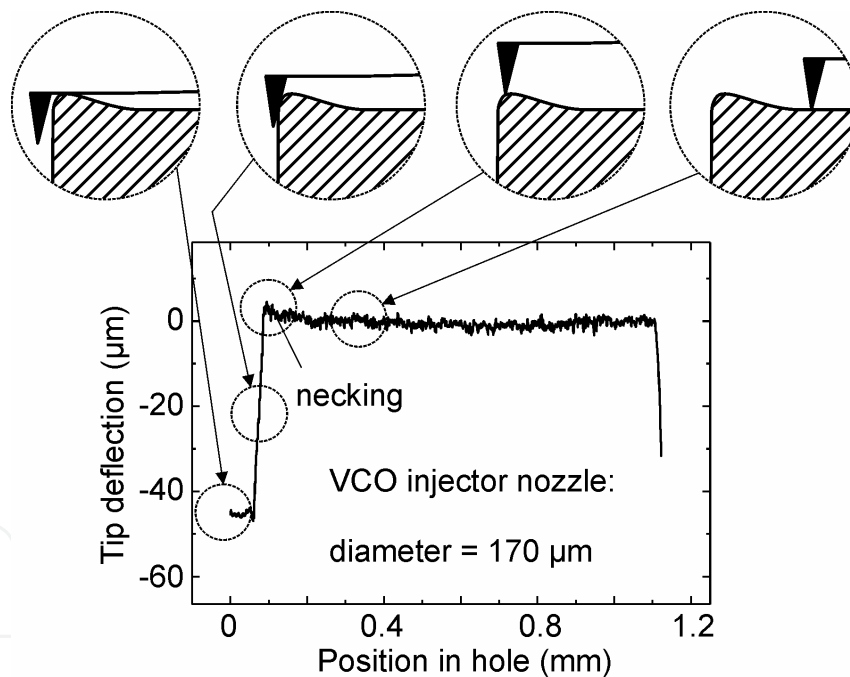


Fig. 15. Typical surface profile measured by scanning within a spray hole of a VCO Diesel injector nozzle using a slender cantilever sensor (lower). The schematics represent the different contact scenarios of the probe about the inlet edge.

In Fig. 16a the profiles from subsequent in-hole scans along identical traces are shown revealing good agreement as indicated by the occurrence of characteristic signatures at identical positions. The profiles provide information on roughness and waviness of the profiles being a measure of the quality of tool and the machine, respectively. Exemplarily, roughness parameters and waviness profile were determined from one of the measured profiles according to ISO 4287 and displayed in Table 5 and Fig. 16b, respectively.

Parameter	Value
$R_p$	1859.27 nm
$R_v$	2716.97 nm
$R_{max}$	4692.09 nm
$R_z$	4576.24 nm
$R_a$	637.08 nm
$R_q$	744.48 nm
$R_c$	1778.09 nm
$R_{Sm}$	16.72 $\mu\text{m}$
$R_{\Delta q}$	0.4318
$R_{sk}$	-0.321
$R_{ku}$	2.782
$R_t$	4460.39 nm

Table 5. Roughness parameters according to ISO 4287 extracted from the profile of the inner-wall surface of a VCO nozzle spray hole displayed in Fig. 14.

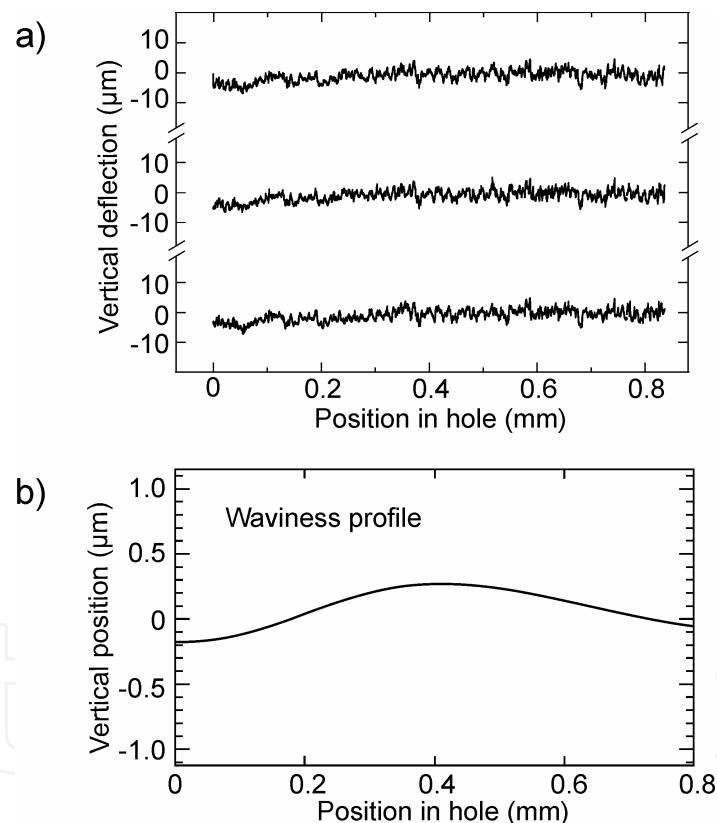


Fig. 16. Surface profiles measured repeatedly along the same trace within a spray hole of a VCO Diesel injector nozzle (a) and waviness profile calculated according to ISO 4287 (b).

Scanning measurements within spray holes were repeated using different sensors at various scanning speeds (2 – 200  $\mu\text{m}/\text{s}$ ) and probing forces. We found good agreement of the signatures in the profiles. Furthermore, the roughness values 0.80, 0.73, 0.76 and 0.74  $\mu\text{m}$  determined at probing speeds of 2, 20, 100, and 200  $\mu\text{m}/\text{s}$  over a scan distance of 300  $\mu\text{m}$  did not show a dependence on probing speed. We conclude that the described piezoresistive cantilever sensors have the potential for fast and non-destructive contour and roughness measurement within spray holes.

## 5. Conclusion

Construction, fabrication and testing of slender piezoresistive cantilever probes were addressed which were designed for tactile shape and roughness measurements with high-aspect-ratio micro components. In the normal cantilever-bending mode the sensor could be operated within an exceptionally large deflection range (hundreds of  $\mu\text{m}$ ) at high scanning speeds ( $>1\text{ mm/s}$ ) and low probing forces ( $<100\ \mu\text{N}$ ). Vertical and lateral resolution amounted to  $\sim 10\text{ nm}$  and  $\sim 1\ \mu\text{m}$ , respectively which fulfils the requirements of form and roughness measurements with machined surfaces. Cross sensitivity vs. temperature and ambient light was typically less than  $10\text{ nm}$  at measurement conditions of temperature and light intensity variations of  $1\text{ K}$  and  $0.1\text{ mW/cm}^2$ , respectively. Sensor response on axial loading could be used for probing the bottom of deep and narrow sac holes. In this case cantilever buckling was normally observed which was monitored by the bridge output to measure the structure heights of 3D-patterned silicon. For the first time form and roughness measurement inside spray holes of injector nozzles could be demonstrated with not sectioned holes. Using tailored prototypes of slender piezoresistive cantilever sensors good reproducibility was obtained at different scanning speeds and loading forces. We could demonstrate the feasibility of slender piezoresistive cantilever sensors for fast, non-destructive and high-performance form and roughness measurements with deep and narrow micro holes.

## 6. Acknowledgements

The author is grateful to the valuable technical assistance by Nadine Beckmann, Doris Rümmler, Julian Kähler and Stefan Kahmann. This work was supported in part by the German Federal Ministry of Education and Research (BMBF) in the framework of the collaborative project "Prüfung und Bewertung geometrischer Merkmale in der Mikrosystemtechnik ( $\mu\text{geoMess}$ )" within the cluster MSTPrüf under no. 16SV1944.

## 7. References

- Anantharamaiah, N.; Vahedi Tafreshi, H. & Pourdeyhimi, B. (2007). A simple expression for predicting the inlet roundness of micro-nozzles. *J. Micromech. Microeng.*, Vol. 17, N31–N39
- Bae, C.; Yu, J.; Kang, J.; Kong, J. & Lee, K.-O. (2002). Effect of Nozzle Geometry on the Common-Rail Diesel Spray. *SAE Techn. Pap. Ser.* 2002-01-1625
- Bao, M.-H. (2000). *Micro Mechanical Transducers*, Elsevier, ISBN 0-444-50558-X, Amsterdam
- Baron, N.; Passave, J.; Guichardaz, B. & Cabodevila, G. (2008). Investigations of development process of high hollow bevelled microneedles using a combination of ICP RIE and dicing saw. *Microsyst. Technol.* DOI 10.1007/s00542-008-0596-1
- Bauza, M. B.; Hocken, R. J.; Smith, S. T. & Woody, S. C. (2005). Development of a virtual probe tip with an application to high aspect ratio microscale features. *Rev. Sci. Instrum.*, Vol. 76, 095112
- Behrens, I.; Doering, L. & Peiner, E. (2003). Piezoresistive cantilever as portable micro force calibration standard. *J. Micromech. Microeng.*, Vol. 13, 1279-1288
- Beyeler, F.; Muntwyler, S.; Nagy, Z.; Graetzel, C.; Moser, M; & Nelson, B. J. (2008). Design and calibration of a MEMS sensor for measuring the force and torque acting on a magnetic microrobot. *J. Micromech. Microeng.* Vol. 18, 025004 (7pp)

- Bos, E. J. C. ; Heldens, R. W. P.; Delbressine, F. L. M.; Schellekens, P. H. J. & Dietzel, A. (2007) Compensation of the anisotropic behavior of single crystalline silicon in a 3D tactile sensor. *Sens. Actuat. A* , Vol.134, 374–381
- Bos, E. J. C.; Delbressine, F.L.M. & Haitjema, H. (2004). High-Accuracy CMM Metrology for Micro Systems, *Proceedings of 8th International Symposium on Measurement and Quality Control in Production, ISMQ2004*, pp. 511-522, Erlangen, Germany, October, 2004, VDI, Düsseldorf, Germany, No. 1860
- Cho, C. H.; Jaeger, R. C. & Suhling, J. C. (2006). Experimental Characterization of the Temperature Dependence of the Piezoresistive Coefficients of Silicon, *Proceedings of ITerm 2006*, pp. 928–935, San Diego, CA , May, 2006
- Choudhury, A.; Hesketh, P. J.; Thundat, T. G.; Hu, Z. & Vujanic, R. (2007). Design and Testing of Single and Double Sided Cantilevers for Chemical Sensing”, *Proceedings of IEEE Sensors 2007 Conf.*, pp. 1432-143, Atlanta, GA, October, 2007
- Cusanelli, G.; Minello, M.; Torchia, F.; Ammann, W. & Grize, P. E. (2007). Properties of Micro-Holes for Nozzle by Micro-EDM, *Proceedings of 15th Intern. Symp. Electromachining (ISEM XV)*, pp. 241-245, Pittsburgh, PA, April, 2007, ISBN (13): 978-0-9794977-0-4
- Diver, C.; Atkinson, J.; Helml, H. J. & Li, L. (2004). Micro-EDM drilling of tapered holes for industrial applications. *J. Mater. Process. Technol.*, Vol. 149, 296–303
- Engelke, R.; Ahrens, G.; Arndt-Staufenbiehl, N.; Kopetz, S.; Wiesauer, K.; Löchel, B.; Schröder, H.; Kastner, J.; Neyer, A.; Stifter, D. & Grützner, G. (2007). Investigations on possibilities of inline inspection of high aspect ratio microstructures. *Microsyst. Technol.*, 13, Vol. 319–325
- Hon, R.; Lee, S. W. R.; Zhang, S. X. & Wong; C. K. (2005). Multi-Stack Flip Chip 3D Packaging with Copper Plated Through-Silicon Vertical Interconnection, *Proceedings of 7th Electron. Packaging Technol. Conf.*, (EPTC 2005), Vol. 2, pp. 384-389, Singapore, December, 2005
- Jung, J.-W.; Ko, S. H.; Jeong, Y. H.; Min, B.-K. & Lee, S. J. (2007). Estimation of Material Removal Volume of a Micro-EDM Drilled Hole Using Discharge Pulse Monitoring. *Int. J. Precision Eng. Manufact.* Vol. 8, 45-49
- Jung, D.; Wang, W. L.; Knafl, A.; Jacobs, T. J.; Hu, S. J. & Assanis, D. N. (2008). Experimental investigation of abrasive flow machining effects on injector nozzle geometries, engine performance, and emissions in a DI Diesel engine. *Intern. J. Automotivoe Technol.*, Vol. 9, No. 1, 9-15
- Kao, C.-C. & Shih, A. J. (2007). Form measurements of micro-holes. *Meas. Sci. Technol.*, Vol. 18, 3603–3611
- Kiuchi, M.; Matsui, S. & Isono, Y. (2008) The piezoresistance effect of FIB-deposited carbon nanowires under severe strain. *J. Micromech. Microeng.*, Vol, 18, 065011 (10pp).
- Krüger, O.; Schöne, G.; Wernicke, T.; John, W.; Würfl, J. & Tränkle, G. (2007). UV laser drilling of SiC for semiconductor device fabrication. *J. Phys.: Conf. Ser.*, Vol. 59, 740–744
- Küng, A.; Meli, F. & Thalmann, R. (2007). Ultraprecision micro-CMM using a low force 3D touch probe. *Meas. Sci. Technol.*, Vol. 18, 319–327
- Lebrasseur, E.; Pourciel, J. P.; Bourouina, T.; Masuzawa, T. & Fujita, H. (2002). A new characterization tool for vertical profile measurement of high-aspect-ratio microstructures. *J. Micromech. Microeng.*, Vol. 12, 280-285
- Li, X.; Wang, J. & Li W. (2007). Current State and Prospect of Micro-Machining, *Proceedings of IEEE Intern. Conf. Automation and Logistics*, pp. 1414-1419, Jinan, China, August, 2007
- Muralikrishnan, B.; Stone, J. A. & Stoup, J. R. (2006). Fiber deflection probe for small hole metrology. *Precision Engineering* Vol. 30, 154-164.

- Mathieu, F.; Saya, D.; Bergaud, C. & Nicu, L. (2007). Parallel Detection of Si-Based Microcantilevers Resonant Frequencies Using Piezoresistive Signals Downmixing Scheme. *IEEE Sens. J.*, Vol. 7, 172–178.
- Nesterov, V. & Brand, U. (2006). Modelling and investigation of the mechanical and electrical characteristics of the silicon 3D-boss microprobe for force and deflection measurements. *J. Micromech. Microeng.*, Vol. 16, 1116–1127
- Peggs, G.; Lewis A. & Oldfield S. (1999). Design for a compact high-accuracy CMM. *CIRP Annals - Manufacturing Technology*, Vol. 48, No. 1, 417–420
- Peiner, E.; Balke, M. & Doering, L. (2007). Slender Tactile Sensor for High-Aspect-Ratio Micro Metrology, pp. 760–763, Proceedings of IEEE Sensors 2007 Conf., Atlanta, GA, October, 2007
- Peiner, E.; Doering, L. & Nesterov, V. (2004). Tactile Probes for High Aspect Ratio Micrometrology. *mstnews*, No. 02/2004, 41,42
- Peiner, E.; Doering, L.; Balke, M. & Christ A. (2008). Silicon Cantilever Sensor for Micro-/Nanoscale Dimension and Force Metrology. *Microsyst. Technol.*, Vol. 14, 441–451
- Pourciel, J.-B.; Jalabert, L. & Masuzawa, T. (2003). Profile and Surface Measurement Tool for High Aspect-Ratio Microstructures. *JSME Intern. J. Series C*, Vol. 46, 916–922
- Rauh, W. (2005). Präzision mit gläserner Faser. *Mikroproduktion*, No. 1/2005, 1–6, Carl Hanser, München, Germany
- Ruther, P.; Spinner, S.; Cornils, M. & Paul, O (2007). Cantilever-based tactile sensor with improved sensitivity for dimensional metrology of deep narrow drillings. *Proceedings of 14th Intern. Conf. Solid-State Sensors, Actuators and Microsystems, (Transducers & Eurosensors '07)*, pp. 1469–1472, Lyon, France, June, 2007
- Samuel, B. A.; Desai, A. V. & Haque, M. A. (2006). Design and modeling of a MEMS pico-Newton loading/sensing device. *Sens. Actuators A*, Vol. 127, 155–162
- Seitz, K. (2005). Qualitätsprüfung in der Mikrosystemtechnik. *inno*, Vol. 29, No. 03/05, 19, IVAM, Dortmund, Germany
- Seo, T.-I.; Kim, D.-W.; Cho, M.-W. & Lee, E.-S. (2008). A Study on the Characteristics of Micro Deep Hole Machining Processes. *Key Engineering Materials*, Vols. 364–366, 566–571, Trans Tech Publications, Switzerland
- Simon, M.; Reznikova, E.; Nazmov, V. & Last, A. (2008). Measurement of side walls of high aspect ratio microstructures. *Microsyst. Technol.* DOI 10.1007/s00542-008-0618-z
- Tibrewala, A.; Phataralaoha, A.; & Büttgenbach, S. (2008). Analysis of full and cross-shaped boss membranes with piezoresistors in transversal strain configuration. *J. Micromech. Microeng.*, Vol. 18, 055001 (6pp)
- UMAP (2008) Vision System, Catalog No. E4257-361, Mitutoyo Corporation, Japan. Available: <http://www.mitutoyo.co.jp>
- Vora, K. D.; Shew, B.-Y.; Lochel, B.; Harvey, E. C.; Hayes, J. P. & Peele, A. G. (2008). Sidewall slopes and roughness of SU-8 HARMST. *Microsyst. Technol.*, DOI 10.1007/s00542-007-0506-y
- Weckenmann, A.; Peggs, G. & Hoffmann, J. (2006). Probing systems for dimensional micro- and nano-metrology. *Meas. Sci. Technol.*, Vol. 17, 504–509
- Woody, S. C. & Bauza, M. B. (2007). High Aspect Ratio Sensors with an application Application to microscale Metrology, *Proc. 2007 NCSL Intern. Workshop & Symp. on Metrology's Impact on Products and Services*. Available: <http://www.x-cd.com/ncsli07/search.html>
- Yamamoto, M.; Takeuchi, H. & Aoki, S. (2000). Dimensional measurement of high aspect ratio micro structures with a resonating micro cantilever probe. *Microsyst. Technol.*, Vol. 6, 179–83



### **Sensors: Focus on Tactile Force and Stress Sensors**

Edited by Jose Gerardo Rocha and Senentxu Lanceros-Mendez

ISBN 978-953-7619-31-2

Hard cover, 444 pages

**Publisher** InTech

**Published online** 01, December, 2008

**Published in print edition** December, 2008

This book describes some devices that are commonly identified as tactile or force sensors. This is achieved with different degrees of detail, in a unique and actual resource, through the description of different approaches to this type of sensors. Understanding the design and the working principles of the sensors described here requires a multidisciplinary background of electrical engineering, mechanical engineering, physics, biology, etc. An attempt has been made to place side by side the most pertinent information in order to reach a more productive reading not only for professionals dedicated to the design of tactile sensors, but also for all other sensor users, as for example, in the field of robotics. The latest technologies presented in this book are more focused on information readout and processing: as new materials, micro and sub-micro sensors are available, wireless transmission and processing of the sensorial information, as well as some innovative methodologies for obtaining and interpreting tactile information are also strongly evolving.

#### **How to reference**

In order to correctly reference this scholarly work, feel free to copy and paste the following:

Erwin Peiner (2008). Compliant Tactile Sensors for High-Aspect-Ratio Form Metrology, *Sensors: Focus on Tactile Force and Stress Sensors*, Jose Gerardo Rocha and Senentxu Lanceros-Mendez (Ed.), ISBN: 978-953-7619-31-2, InTech, Available from: [http://www.intechopen.com/books/sensors-focus-on-tactile-force-and-stress-sensors/compliant\\_tactile\\_sensors\\_for\\_high-aspect-ratio\\_form\\_metrology](http://www.intechopen.com/books/sensors-focus-on-tactile-force-and-stress-sensors/compliant_tactile_sensors_for_high-aspect-ratio_form_metrology)

**INTECH**  
open science | open minds

#### **InTech Europe**

University Campus STeP Ri  
Slavka Krautzeka 83/A  
51000 Rijeka, Croatia  
Phone: +385 (51) 770 447  
Fax: +385 (51) 686 166  
[www.intechopen.com](http://www.intechopen.com)

#### **InTech China**

Unit 405, Office Block, Hotel Equatorial Shanghai  
No.65, Yan An Road (West), Shanghai, 200040, China  
中国上海市延安西路65号上海国际贵都大饭店办公楼405单元  
Phone: +86-21-62489820  
Fax: +86-21-62489821

© 2008 The Author(s). Licensee IntechOpen. This chapter is distributed under the terms of the [Creative Commons Attribution-NonCommercial-ShareAlike-3.0 License](#), which permits use, distribution and reproduction for non-commercial purposes, provided the original is properly cited and derivative works building on this content are distributed under the same license.

IntechOpen

IntechOpen